1

## **Imaging the Hydrothermal System of Kirishima Volcanic Complex, Japan with L-band**

## **InSAR Time Series**

**Zhang Yunjun[1,†], Falk Amelung[1], and Yosuke Aoki[2]**


[1]Rosentiel School of Marine and Atmospheric Science, University of Miami, Miami, FL, USA.

[2]Earthquake Research Institute, University of Tokyo, Tokyo, Japan.

[†]Now at Seismological Laboratory, California Institute of Technology, Pasadena, CA, USA.

Corresponding author: Z. Yunjun (yunjunzgeo@gmail.com)

**Key Points:**

- Shinmoe-dake hydrothermal system deflated during the 2008-2010 eruptions, then was replaced by a magmatic body during the 2011 eruption.

- Persistent inflation at the Iwo-yama crater during 2014-2019 is driven by liquid-gas two-phase water boiling.

- Precursory expansion of Iwo-yama's southern and western vents after December 2017 is driven by the upward migration of magmatic fluid.

**Abstract**

We present deformation measurements of the Kirishima volcanic complex from ALOS and ALOS-2 Interferometric Synthetic Aperture Radar (InSAR) time-series during 2006-2019. Shinmoe-dake deflated ~6 cm during the 2008-2010 phreatic eruptions and inflated ~5 cm prior to the 2017 magmatic eruption. Iwo-yama inflated ~19 cm within the crater since January 2015 and ~7 cm around the southern and western vents since four months before the 2018 eruption. These deformations can be modeled as ellipsoids at ~700 m depth beneath Shinmoe-dake and as a sphere on top of an ellipsoid at ~130 and ~340 m depths beneath Iwo-yama. Combining geodetic, geoelectric, geochemical and petrological analysis, we interpret the hydrothermal origin of the deflation at Shinmoe-dake and inflation at Iwo-yama; the hydrothermal-magmatic transition during the 2011 Shinmoe-dake eruption; water-boiling and bottom-up pressurization as driving mechanisms of the inflation at Iwo-yama. The study highlights the imaging potential of InSAR time-series on complex hydrothermal systems.

**Plain Language Summary**

Steam-blast eruptions are driven by the heat of magma interacting with water. Although small in size, they are very common and unpredictable, making them hazardous. In order to know when and where these interactions started and how they led to the eruption, we take the Kirishima volcano group as an example and use 10 years of satellite radar images to measure its ground surface deformation. We find that Shinmoe-dake fell ~6 cm during the 2008-2010 eruptions, much earlier than previously thought; while Iwo-yama rose ~7 cm since four months before its 2018 eruption. Combining models from specialized computer code with previous studies from other disciplines, we explain the fall of Shinmoe-dake and the rise of Iwo-yama are due to the steam release and water accumulation of water-rich zones at ~700 m and ~340 m depth below

39   the surface, respectively. The water-rich zone of Shinmoe-dake was replaced and filled by

40   magma during the 2011 eruption. These short-lived, small-size deformations have not been

41   identified in the region before, nor has the type of deformation in general been studied

42   extensively worldwide. Future volcano monitoring efforts should take this into account on a

43   regular basis.

44   **1 Introduction**

45   Phreatic eruptions are among the most common but also among the most unpredictable

46   volcanic phenomena, making them hazardous despite the relatively small scale. Unlike magmatic

47   eruptions driven by magma migration, volatile exsolution and crystallization, phreatic eruptions

48   are driven by broadly defined hydrothermal processes, such as interactions among water, rocks

49   and magmatic heat and gas, similar to geyser-like mechanisms but more violent with the

50   expulsion of rocks and mud, usually without juvenile material (Germanovich & Lowell, 1995;

51   Muffler et al., 1971; Stix & Moor, 2018).  Many of the largest volcanic eruptions started with

52   phreatic events, e.g. the 1980 Mt. St. Helens eruption (Christiansen et al., 1982) and the 1991

53   Pinatubo eruption (Newhall & Punongbayan, 1996), but phreatic eruptions may also occur in

54   isolation.

55   Geophysical monitoring of phreatic eruptions has been challenging due to their localized

56   deformation signals with small magnitude and sudden occurrence with few if any precursors

57   (Kobayashi et al., 2018). Although not as frequently as magmatic processes, ground deformation

58   associated with hydrothermal processes has been observed in all stages of volcanic eruption

59   cycles, including the pre-eruptive (Kobayashi et al., 2018; Narita et al., 2020), co-eruptive

60   (Himematsu et al., 2020), post-eruptive period (Hamling et al., 2016; Nakaboh et al., 2003;

61 Narita & Murakami, 2018) and non-eruptive unrest period (Battaglia et al., 2006; Lu et al., 2002;

62 Lundgren et al., 2001).

63      Here we report a decade-long Interferometric Synthetic Aperture Radar (InSAR)

64 deformation time-series of the Kirishima volcanic complex, Japan during 2006-2011 and 2014-

65 2019, covering the 2008 and 2017 Shinmoe-dake eruptions and the 2018 Iwo-yama eruption. We

66 estimate the location, geometry and volume change of the pressure sources and combine them

67 with previous observations from resistivity, geochemistry and petrology to a new model for the

68 shallow plumbing system of the central Kirishima volcanoes.

## 69   2 Geological Setting

70      The Kirishima volcanic complex (Japanese for foggy mountain) is located in southern

71 Kyushu, where the Phillippine Sea Plate is subducted beneath the Amurian Plate (Wallace et al.,

72 2009). The complex consists of more than 25 craters, cones and lava domes produced by the

73 southward migration of eruption centers in the last 330 ka (Fig. 1a; Nakada et al., 2013). These

74 volcanic centers form an elliptical 30 by 20 km northwest-trending zone with younger volcanism

75 generally in the southeast (Chapman et al., 2009). The most active eruptive centers are Iwo-yama

76 (Japanese for sulfur peak), Shinmoe-dake and Ohachi (altitudes of 1,313 m, 1,421 m and 1,408

77 m, respectively). Hydrothermal systems are widely distributed in shallow levels throughout

78 Kirishima (e.g., Aizawa et al., 2014; Ohba et al., 1997). It has been suggested that the magmatic

79 system beneath connects at depth with Aira caldera located 20 km to the south (Brothelande et

80 al., 2018).

81      The 2011 Shinmoe-dake eruption is the first magmatic eruption in the complex since its

82 1716-17 eruption. Other eruptions at Shinmoe-dake in 1822, 1959 and 1991 are phreatic (Imura

83 & Kobayashi, 1991). Iwo-yama, the youngest volcanic center, was formed in the 16th-17th

84  century and had a phreatic eruption in 1768 (Tajima et al., 2014). Ohachi had a series of

85  eruptions between 1880 and 1923 (GVP, 2013).

**3 The 2008-2019 Activity**

87      The unrest of Shinmoe-dake started with a substantial increase in seismicity and a rapid

88  strain change three days before the first phreatic eruption on 22 August 2008 when a lake was

89  present in the crater (Geshi et al., 2010; Yamazaki et al., 2020). Additional phreatic eruptions

90  occurred from March to July 2010 (solid blue line/box in Fig. 1i). The 2011 eruption started with

91  a phreatomagmatic eruption on 19 January and three sub-Plinian eruptions on 26-27 January,

92  followed by stages of lava extrusion, Vulcanian and phreatomagmatic eruptions until September

93  (Nakada et al., 2013). Shinmoe-dake had new magmatic eruptions on 11-17 October 2017 and 1

94  March to 27 June 2018 (solid orange line/box in Fig. 1i; GVP, 2013).

95      In December 2009, more than a year after the first phreatic eruption, GPS and InSAR

96  data showed inflation over the western flank of the volcanic complex that was attributed to an

97  inflating pressure source beneath Ebino-dake at ~10 km depth (dashed circle in Fig. 1a; Fig. 1h;

98  Nakao et al., 2013; Miyagi et al., 2013). Rapid strain change is reported three days before this

99  inflation (Yamazaki et al., 2020). The source deflated during the climactic phase of the 2011

100  Shinmoe-dake eruption and re-inflated until November 2011 (Fig. 1h; Nakao et al., 2013; Ueda

101  et al., 2013).

102      About an hour and a half prior to the first sub-Plinian eruption tiltmeter and broadband

103  seismometer recorded localized inflation near the crater suggesting a shallow pressure source

104  (Takeo et al., 2013). In the following two weeks, this source underwent a sequence of inflation-

105  deflation cycles during the sub-Plinian, lava extrusion and Vulcanian stages. The deformation

106  signals, synchronized with volcanic tremors or long-period events, were attributed to the

107 pressurization of a shallow conduit beneath the crater (Nakamichi et al., 2013; Takeo et al.,

108 2013). Localized deflation and inflation patterns were also observed from November 2011 to

109 May 2013 and prior to the 2017 magmatic eruption (Miyagi et al., 2014; Morishita & Kobayashi,

110 2018).

111       The unrest of Iwo-yama started with an increase in seismicity in December 2013,

112 followed by tremors in August 2014, thermal anomalies and weak fumarolic activity since

113 December 2015, a steam blowout event on 27 April 2017 at the crater and small phreatic

114 eruptions on 19 and 20 April 2018 at two newly appeared vents on the southern and western side

115 of the crater with plume heights of 100-200 m (Tajima et al., 2020; dashed blue lines in Fig. 1g-

116 i). Localized pre-eruptive inflation suggests a very shallow pressure source at 150 m depth

117 beneath the crater (Narita et al., 2020). Fumarolic activity and mud ejection continued from the

118 southern and western vents as of December 2019 (JMA, 2019).

119 **4 InSAR Data and Method**

120       We use 2006-2011 ALOS (ascending track 424 and descending track 73) and 2014-2019

121 ALOS-2 (ascending track 131 and descending track 23) L-band stripmap SAR imagery to form

122 small temporal and spatial baseline interferograms (see Fig. S1 and Table S1 for detailed

123 configurations). We remove the topographic phase using the Digital Elevation Model (DEM)

124 released by Geospatial Information Authority of Japan (GSI, 0.4 arc second, ~10 m) and unwrap

125 the phase using the minimum cost flow method (Chen & Zebker, 2001). Ionospheric delays are

126 not corrected.

127       We use the stripmap stack processor (Fattahi et al., 2017) of the ISCE software (Rosen et

128 al., 2012) for interferogram processing and the Miami InSAR time-series software in Python

129 (MintPy) for time series analysis (Yunjun et al., 2019). We exclude low-coherence

130    interferograms using coherence-based network modification with a custom area of interest

131    around Shinmoe-dake (black empty square in Fig. S2) for the average coherence calculation and

132    thresholds of 0.7 for ALOS descending track 73 and 0.8 for the others. We correct for the

133    stratified tropospheric delay using the ERA-5 atmospheric reanalysis model (Copernicus Climate

134    Change Service, 2017; Jolivet et al., 2011), for long spatial-wavelength phase components by

135    removing linear phase ramps from all acquisitions and for topographic residuals due to the DEM

136    error (Fattahi & Amelung, 2013; Fig. S3). We use a temporal coherence threshold of 0.8 to

137    eliminate unreliable pixels. Noisy acquisitions with residual phase root mean squares larger than

138    the predefined cutoff (1 and 2 median absolute deviations for ALOS and ALOS-2, respectively)

139    are excluded during the estimation of topographic residual and average velocity (empty circles in

140    Fig. 1g; Fig. S4).

141    To obtain the optimal InSAR measurement for time periods of interest (Fig. 1d-f), we

142    apply two extra steps in addition to the routine MintPy workflow (Fig. S5-S8). First, to maximize

143    the number of reliable pixels we exclude interferograms with acquisitions after the 2011 and

144    2017 eruptions, which are decorrelated by local processes inside the crater and/or by the newly

145    deposited ash nearby (Fig. S9-S10). Second, to mitigate residual atmospheric turbulence we

146    estimate the linear line-of-sight (LOS) velocities for the time periods of interest and convert them

147    to cumulative displacements instead of using the differential displacement between two

148    acquisitions (see Fig. S11 for a comparison).

149    Within the Shinmoe-dake crater, lava domes from the 2011 and 2017 eruptions dominate

150    the topography change (DEM error) since the DEM generation before 2011. We use the locally

151    referenced DEM errors from ALOS-2 ascending and descending InSAR time-series between the

152    2011 and 2017 eruptions to measure the thickness and volume of the lava dome extruded from

153    the 2011 eruption (see Fig. S12 for details), providing an alternative approach to the SAR

154    intensity simulation and the single-pass SAR interferometry (Ozawa & Kozono, 2013; Shimono

155    et al., 2011).

**5 Results**

157        We obtain the quasi-vertical displacements from ascending and descending data (Wright

158    et al., 2004) during 2006-2019 to examine the deformation at the Kirishima volcanic complex

159    and find five distinct spatial patterns: three at Shinmoe-dake and two at Iwo-yama during three

160    different time periods (Fig. 1d-f; Fig. S13-S15). Shinmoe-dake deflated ~6 cm between the

161    2008-2010 phreatic eruptions (blue colors in Fig. 1d), inflated ~5 cm prior to the 2017 magmatic

162    eruption (yellow-red colors in Fig. 1e) and has been deflating since the end of the 2018

163    magmatic eruption (Fig. 1f). Iwo-yama did not show any signal before 2011 (Fig. 1d) but has

164    been inflating since at least January 2015. The deformation is localized and concentrated on the

165    crater area during 2015-2017 (Fig. 1e), then expanded to a larger area in December 2017 (Fig.

166    1f), four months prior to the April 2018 phreatic eruption (dashed blue line in Fig. 1g) when new

167    vents appeared on the southern and western side of the crater.

168        The LOS displacement time-series show temporal details (Fig. 1g). At Shinmoe-dake, the

169    eastern crater rim (point A) shows no noticeable deformation prior to the 2008 phreatic eruption

170    (solid blue line) and ~6 cm of linear LOS decrease (subsidence) between the 2008-2010 phreatic

171    eruptions; the western crater rim (point B) shows ~4 cm of LOS increase (uplift) prior to the

172    2017 magmatic eruption (solid orange line) and a net ~4 cm of near-linear LOS decrease after

173    the 2018 magmatic eruption. At Iwo-yama, the crater (point C) shows ~19 cm of near-linear

174    LOS increase during 2014-2019 while the southern and western vents (points S and W) show no

175    significant displacement before December 2017 but ~5 and ~7 cm of LOS increases afterward.

176  This horizontal expansion since December 2017 coincides with the increased seismic activity

177  (Fig. 1i). Since the end of 2018, Iwo-yama shows no noticeable displacement except for the

178  vicinity of its western vent where linear LOS increase continues until August 2019.

179      Note that the relatively strong localized inflation on the western summit flank of

180  Shinmoe-dake prior to the 2017 eruption (Fig. 1e) is likely related to a potentially partially

181  solidified fissure from which the previous 2008-2010 eruptions occurred (Geshi et al., 2010). We

182  do not interpret the pre-/co-/post-eruptive deformation of the 2018 Shinmoe-dake eruption as

183  shown in the GPS baseline change (Fig. 1h) due to the overlap with the erupted ash/tephra from

184  the 2017 eruption (Fig. 1f; Fig. S7-S8 and S16). Similar ash/tephra deposits are also observed

185  during the 2011 eruption from phase (Fig. S17) and coherence measurement (Jung et al., 2016).

**6 Modeling**

187      We use geophysical inverse models to constrain sources of deformation at Shinmoe-dake

188  during 2008-2010 and 2015-2017 and at Iwo-yama during 2015-2017 and 2017-2019. We

189  assume an isotropic elastic half-space and use the vectorized finite compound dislocation models

190  (CDM), composed of three mutually orthogonal rectangular dislocations (with semi-axes

191  $a_X, a_Y, a_Z$) with uniform opening and full rotational degrees of freedom (Nikkhoo et al., 2016;

192  see also Beauducel et al., 2020). The CDM model represents a generic ellipsoid eliminating the

193  need to pre-specify the source geometry such as sphere or sill. We substitute two semi-axes

194  $a_Y, a_Z$ of the CDM with their dimensionless ratios to $a_X$ as $a_Y/a_X$ and $a_Z/a_X$, for easier

195  constraints on the source shape if needed. For Shinmoe-dake during 2015-2017 we fixed the

196  shape and orientation of the CDM due to the lack of near-field observations (we eliminated data

197  points inside the crater affected by local processes). For Iwo-yama during 2017-2019 we use two

198  CDMs and fix one of them with the geometry and location inferred from the previous 2015-2017

199  period. Although hydrothermal processes deform the ground in a thermo-poro-elastic fashion,

200  simple elastic models are well suited to infer the source geometric features for deformation from

201  distinct episodic unrest where poroelastic response dominates (Fournier & Chardot, 2012; Lu et

202  al., 2002). If mechanically weak layers are present the sources will be deeper than estimated here

203  (Manconi et al., 2007). We use a Poisson's ratio of 0.25.

204      We account for the elevation effect of the topography using the varying-source depth

205  method (Williams & Wadge, 1998). The height value from GSI DEM is converted from ellipsoid

206  to geoid (31.2 m difference), which is not negligible considering the shallow depth. To fulfill the

207  positive depths requirement of the CDM solution, we apply a minimum free surface height

208  constraint of 1,100 m for Shinmoe-dake and of 1,300 m for Iwo-yama. The impact is negligible

209  for all models except for Iwo-yama during 2017-2019, where the lower source of the two could

210  be shallower (<56 m) than estimated here but within the reported 95% confidence intervals

211  (±100 m; see Table S2 for a detailed evaluation).

212      We jointly invert the ascending and descending InSAR LOS displacement measurements

213  using the Bayesian approach in GBIS (Bagnardi & Hooper, 2018). We subsample the data using

214  a gradient-based adaptive quadtree method (Jónsson et al., 2002) in the near field and use

215  uniform sampling in the far-field (where the signal-to-noise ratio is low; Table S3; Fig. S18-

216  S19). We account for the data uncertainties using structural functions (Lohman & Simons, 2005;

217  Table S3). We use uniform prior probability density functions (PDF) bounded by geologically

218  realistic values. The inversion algorithm samples posterior PDF of source model parameters with

219  1,000,000 iterations. The optimal (maximum a posteriori probability) parameter value and 95%

220  confidence intervals are shown in Table S4. All free model parameters converged well except the

221  semi-axis along the X-axis for Shinmoe-dake during 2015-2017 and the opening of the upper

222    CDM for Iwo-yama during 2017-2019. There are trade-offs between some parameters (see joint

223    PDF in Fig. S20-S23) but do not affect the depth and derived volume change.

224         For Shinmoe-dake, the optimal solution for the 2008-2010 deflation is a slightly inclined

225    prolate ellipsoid (Fig. 2a-e) beneath the northeastern crater section with the centroid at depth of

226    ~620 ± 50 m below the summit (black star in Fig. 2c-d). For the 2015-2017 inflation, the optimal

227    solution is a sphere beneath the crater center at depth of ~730 ± 210 m below the summit (black

228    star in Fig. 2h-i). The estimated cavity volume changes for the two time periods are -124 ± 26 ×

229    $10^3$ m$^3$ and  146 ± 95 × $10^3$ m$^3$, respectively.

230         For Iwo-yama, the optimal solution for the 2015-2017 inflation is a sphere with ~70 m

231    semi-axes at depth of ~130 ± 10 m below the summit with an estimated cavity volume increase

232    of 15 ± 2 × $10^3$ m$^3$. The optimal solution for 2017-2019 inflation is two CDMs on top of each

233    other: one sphere with fixed parameters from the 2015-2017 period except for a free opening

234    bounded by the 95% confidence intervals assuming a constant opening rate and one ellipsoid

235    located at depth of ~340 ± 100 m below the summit with elongated dimension along the east-

236    west direction. The estimated total cavity volume increase is 76 ± 39 × $10^3$ m$^3$.

237    **7 Discussion**

238         The InSAR time-series deformation provides new insights into the shallow volcanic

239    system (within the volcanic edifice) of the central Kirishima volcanoes, in addition to a well-

240    established deep source beneath Ebino-dake at ~10 km depth below the surface.

241         7.1 Shinmoe-dake: Hydrothermal origin of the 2008-2010 deflation

242         The deflation between the 2008-2010 phreatic eruptions is of hydrothermal origin, as

243    most of the erupted material before March 2010 is hydrothermally altered (<1 vol% of juvenile

244　material; Suzuki et al., 2013). This is consistent with geoelectrical-detected widespread shallow

245　low-resistivity, water-saturated porous layers (e.g. Aizawa et al., 2014). Furthermore, most of the

246　deflation occurred before December 2009 when the deep source began to inflate (point A in Fig.

247　1g).

248　　　　The prolate geometry from geodetic modeling could indicate the depressurization of a

249　former magmatic conduit. The estimated cavity volume decrease ($124 \pm 26 \times 10^3$ m$^3$) is similar

250　to the volume of erupted tephra ($120 \times 10^3$ m$^3$; Geshi et al., 2010) from the August 2008

251　eruption. No noticeable co-eruptive deformation is observed from InSAR (point A in Fig. 1g). A

252　possible mechanism is that the August 2008 eruption unsealed the system and emptied the

253　reservoir, which was immediately refilled by hydrothermal fluids; these fluids were released via

254　steam emission (JMA, 2019) during 2008-2010, resulting in surface subsidence.

255　　　　7.2 Shinmoe-dake: Replacement of hydrothermal system by magmatic body

256　　　　The 2015-2017 inflation prior to a magmatic eruption was almost certainly magmatic, as

257　indicated by the elevated SO$_2$ emission higher than the background level since 2011 (JMA,

258　2019). The inferred depth of 730 m is very similar to 2008-2010 (overlapping PDFs in Fig. 3a).

259　A similar source depth was also inferred for the Vulcanian stage of the 2011 magmatic eruption

260　(Takeo et al., 2013) and for November 2011 to May 2013 magma extrusion period (Miyagi et al.,

261　2014). These depths suggest that the deflation/inflation during the above four periods are from

262　the same source. Together, the similar geodetic source depths, the appearance and dominance of

263　SO$_2$ fluxes and juvenile materials from ash samples suggest that part of the porous rock mass that

264　acted as a hydrothermal source in 2008-2010 was replaced by a magmatic body during the 2011

265　eruption and stayed as magmatic since then. This is similar to the 2014-2015 phreatic-magmatic

266  transitions in Turrialba volcano inferred from gas emission data (de Moor et al., 2016) but at a

267  much shallower level and transited only once.

268  7.3 Iwo-yama: Triple-source hydrothermal system

269  The expanded inflation at Iwo-yama since December 2017 cannot be explained by the

270  single source at 130 m depth (very well constrained with a 95% confidence interval of <10 m

271  due to the shallow depth and coherent near-/far-field observation). Geodetic modeling suggests

272  an extra east-west oriented lay-down cigar-shaped source further down at depth of 340 m (Fig.

273  2p-t and 3b) with two sources on top of each other at very shallow depths prior to the eruption.

274  Both sources are hydrothermal as evident from the strong fumarolic activity, steam emissions,

275  and ejection of mud and hot water since 2014 (JMA, 2019).

276  The upper source at 130 m depth (1180 m a.s.l.) has been inflating since at least January

277  2015 (point C in Fig. 1g). There is a minor peak location change during 2016-2018 around the

278  Iwo-yama crater (Narita et al., 2020). Geochemical analysis in 2016 shows that the water is

279  meteoric (Tajima et al., 2020), suggesting the upward migration of magmatic fluid is not the

280  primary direct driver. Geoelectric surveys have resolved a low-resistivity zone at 200-700 m

281  depth (Tsukamoto et al., 2018), which is below the upper source thus can not serve as caprocks

282  for hydrothermal sealing to support persistent overpressure. The fumarolic temperature has

283  continuously been around or above 96 °C (Tajima et al., 2020), which is the water boiling point

284  temperature at 1180 m a.s.l. Thus, we conclude that the liquid-gas two-phase boiling of meteoric

285  water is the primary driver of the persistent localized inflation around the Iwo-yama crater.

286  The lower source at 340 m depth hosts the southern and western vents and is responsible

287  for the April 2018 eruption. Considering 1) the mix of meteoric and magmatic water and the

288  sharp increase of $SO_2$ and $H_2$ concentrations in fumarolic gas from the geochemical analysis in

289  2018 before the eruption and 2) the observation of days of fluid upwelling just before the 2017

290  blowout and 2018 eruption (Ohba et al., 2021; Tajima et al., 2020), we interpret the expanded

291  inflation is driven by the bottom-up pressurization from the upward migration of magmatic fluid.

292  The magmatic fluid is likely generated by the interaction between local meteoric water and

293  magmatic vapor rising from the depth (Ohba et al., 2021).

294      Residuals of geodetic modeling show a localized uplift at the western vent after

295  December 2017 (Fig. S24 and the difference between solid lines and empty circles in Fig. 2t).

296  The small spatial scale (~150 m in diameter) and the exact same location from ascending and

297  descending orbits suggest the corresponding pressure source is even shallower than the one at

298  130 m depth. In total, Iwo-yama hosts a complex hydrothermal system with three tiny reservoirs

299  at very shallow depths.

300      7.4 Conceptual model of the Kirishima plumbing system

301      The magmatic and hydrothermal plumbing system of the Kirishima volcanic complex is

302  summarized in Fig. 3c. A deep (~10 km below the surface) magmatic source beneath Ebino-dake

303  inflated between December 2009 and the 2011 eruption (Fig. S17) and inflated again between

304  the 2017 and 2018 eruption (Fig. 1h). The shallow source beneath Shinmoe-dake (~700 m below

305  the summit) was hydrothermally evacuating gas and steam between the 2008-2010 phreatic

306  eruptions, then turned magmatic during the 2011 eruption and has been accumulating magma

307  since at least January 2015, feeding the 2017 and 2018 magmatic eruptions. The very shallow

308  hydrothermal reservoir beneath Iwo-yama (130 m below the summit) has been boiling since at

309  least January 2015. In December 2017 another slightly deeper hydrothermal reservoir (340 m

310  below the summit) started accumulating magmatic fluid, feeding the April 2018 phreatic

311  eruption. These shallow hydrothermal reservoirs beneath Iwo-yama are possibly connected to the

312    subvertical conductor (2-10 km b.s.l.; Aizawa et al., 2014) via magma degassing and

313    hydrothermal fluid migration (Ohba et al., 2021; Tsukamoto et al., 2018), thus, sharing the same

314    origin of deep magmatic source with Shinmoe-dake.

315    **8 Conclusions**

316    We derived the surface deformation history of the Kirishima volcanic complex during

317    2006-2011 and 2014-2019 using InSAR time series analysis. Built upon the routine workflow,

318    we demonstrated that excluding interferograms after destructive eruptions and using average

319    velocity could increase the spatial coverage of near-field observation and further beat down the

320    residual tropospheric turbulence after tropospheric correction, to improve the displacement

321    estimate for time periods of interest. We also described a new approach for lava dome mapping

322    using DEM errors from time series analysis.

323    Combining geodetic and petrologic data, we identified the hydrothermal reservoir

324    beneath Shinmoe-dake subsiding after the August 2008 eruption, much earlier than the

325    previously thought precursory magmatic inflation since December 2009. The compilation of

326    multiple geodetic studies suggests this hydrothermal reservoir is replaced by a magmatic body

327    during the 2011 eruption. At Iwo-yama, the deformation time-series reveals a precursory

328    horizontal expansion for the 2018 eruption. We propose a hydrothermal system with three tiny

329    reservoirs beneath Iwo-yama at very shallow levels to explain the observed deformation.

330    Combining geodetic, geoelectric and geochemical data, we conclude that the deformation is

331    driven by liquid-gas two-phase boiling of meteoric water at the upper reservoir and bottom-up

332    pressurization from upward migration of magmatic water at the lower reservoir. The study

333    highlights the imaging potential of InSAR time-series for complex hydrothermal systems and the

334    importance of multidiscipline data for understanding volcanic processes.

**Data and Code Availability**

The InSAR displacement products and geodetic modeling results are available on Zenodo

(https://doi.org/10.5281/zenodo.4661725, https://doi.org/10.5281/zenodo.4499238 and

https://doi.org/10.5281/zenodo.4499208). Figures are prepared using GMT (Wessel et al., 2013)

and Matplotlib (Hunter, 2007) in Jupyter Notebook available on Zenodo

(https://doi.org/10.5281/zenodo.4661735).

**References**

Aizawa, K., et al. (2014), Three-dimensional resistivity structure and magma plumbing system of the

Kirishima Volcanoes as inferred from broadband magnetotelluric data, *Journal of Geophysical

Research: Solid Earth*, *119*(1), 198-215, doi:10.1002/2013jb010682.

Bagnardi, M., and A. Hooper (2018), Inversion of Surface Deformation Data for Rapid Estimates of

Source Parameters and Uncertainties: A Bayesian Approach, *Geochemistry, Geophysics, Geosystems*,

*19*, doi:10.1029/2018GC007585.

357    Battaglia, M., C. Troise, F. Obrizzo, F. Pingue, and G. De Natale (2006), Evidence for fluid migration as

358         the source of deformation at Campi Flegrei caldera (Italy), *Geophysical Research Letters*, *33*(1),

359         doi:10.1029/2005GL024904.

360    Beauducel, F., A. Peltier, A. Villié, and W. Suryanto (2020), Mechanical Imaging of a Volcano Plumbing

361         System From GNSS Unsupervised Modeling, *Geophysical Research Letters*, *47*(17),

362         e2020GL089419, doi:10.1029/2020GL089419.

363    Brothelande, E., F. Amelung, Z. Yunjun, and S. Wdowinski (2018), Geodetic evidence for

364         interconnectivity between Aira and Kirishima magmatic systems, Japan, *Scientific Reports*, *8*(1),

365         9811, doi:10.1038/s41598-018-28026-4.

366    Chapman N., Apted M., Beavan J., Berryman K., Cloos M., Connor C. et al. (2009), Development of

367         Methodologies for the Identification of Volcanic and Tectonic Hazards to Potential HLW Repository

368         Sites in Japan: the Kyushu Case Study, in *NUMO-TR-09-02*, edited, Nuclear Waste Management

369         Organization of Japan.

370    Chen, C. W., and H. A. Zebker (2001), Two-dimensional phase unwrapping with use of statistical models

371         for cost functions in nonlinear optimization, *JOSA A*, *18*(2), 338-351,

372         doi:10.1364/JOSAA.18.000338.

373    Christiansen, R. L., D. W. Peterson, P. Lipman, and D. Mullineaux (1981), Chronology of the 1980

374         eruptive activity, *US Geol. Surv. Prof. Pap*, *1250*, 17-30, doi:10.3133/pp1250.

375    Copernicus Climate Change Service (2017): ERA5: Fifth generation of ECMWF atmospheric reanalyses

376         of the global climate. *Copernicus Climate Change Service Climate Data Store*, date of access: 3 June

377         2019. https://cds.climate.copernicus.eu/cdsapp#!/home

378    de Moor, J. M., et al. (2016), Turmoil at Turrialba Volcano (Costa Rica): Degassing and eruptive

379         processes inferred from high-frequency gas monitoring, *Journal of Geophysical Research: Solid

380         Earth*, *121*(8), 5761-5775, doi:10.1002/2016jb013150.

381    Fattahi, H., and F. Amelung (2013), DEM Error Correction in InSAR Time Series, *Geoscience and

382         Remote Sensing, IEEE Transactions on*, *51*(7), 4249-4259, doi:10.1109/TGRS.2012.2227761.

383  Fattahi, H., M. Simons, and P. Agram (2017), InSAR Time-Series Estimation of the Ionospheric Phase

384     Delay: An Extension of the Split Range-Spectrum Technique, *IEEE Transactions on Geoscience and*

385     *Remote Sensing*, *55*(10), 5984-5996, doi:10.1109/TGRS.2017.2718566.

386  Fournier, N., and L. Chardot (2012), Understanding volcano hydrothermal unrest from geodetic

387     observations: Insights from numerical modeling and application to White Island volcano, New

388     Zealand, *Journal of Geophysical Research: Solid Earth*, *117*(B11), doi:10.1029/2012jb009469.

389  Germanovich, L. N., and R. P. Lowell (1995), The mechanism of phreatic eruptions, *Journal of*

390     *Geophysical Research: Solid Earth*, *100*(B5), 8417-8434, doi:10.1029/94jb03096.

391  Geshi, N., S. Takarada, M. Tsutsui, T. Mori, and T. Kobayashi (2010), Products of the August 22, 2008

392     eruption of Shinmoedake Volcano, Kirishima Volcanic Group, Japan, *BULLETIN OF THE*

393     *VOLCANOLOGICAL SOCIETY OF JAPAN*, *55*(1), 53-64, doi:10.18940/kazan.55.1_53 (in Japanese).

394  Goldstein, R. M., and C. L. Werner (1998), Radar interferogram filtering for geophysical applications,

395     *Geophysical Research Letters*, *25*(21), 4035-4038, doi:10.1029/1998GL900033.

396  GVP (Global Volcanism Program) (2013). Kirishimayama (282090) *in* Volcanoes of the World, v. 4.9.0

397     (04 Jun 2020). Venzke, E (ed.). Smithsonian Institution. Downloaded 17 Aug 2020

398     (https://volcano.si.edu/volcano.cfm?vn=282090). https://doi.org/10.5479/si.GVP.VOTW4-2013

399  Hamling, I. J., C. A. Williams, and S. Hreinsdóttir (2016), Depressurization of a hydrothermal system

400     following the August and November 2012 Te Maari eruptions of Tongariro, New Zealand,

401     *Geophysical Research Letters*, *43*(1), 168-175, doi:10.1002/2015gl067264.

402  Himematsu, Y., T. Ozawa, and Y. Aoki (2020), Coeruptive and posteruptive crustal deformation

403     associated with the 2018 Kusatsu-Shirane phreatic eruption based on PALSAR-2 time series analysis,

404     *Earth Planet Sp*, *72*(1), 116, doi:10.1186/s40623-020-01247-6.

405  Hunter, J. D. (2007), Matplotlib: A 2D Graphics Environment, *Computing in Science & Engineering*,

406     *9*(3), 90-95, doi:10.1109/MCSE.2007.55.

407  Imura, R., and T. Kobayashi (1991), Eruptions of Shinmoedake volcano, Kirishima volcano group, in the

408     last 300 years, *Bull. Volcanol. Soc. Jpn*, *36*, 135-148, doi:10.18940/kazan.36.2_135 (in Japanese).

409    JMA (Japan Meteorological Agency) (2019), 2007-2019 Annual Reports of Volcanic Activity at

410    Kirishima, *Volcanic Activity Explanation Material,* http://www.data.jma.go.jp/svd/vois/data/

411    tokyo/STOCK/monthly_v-act_doc/monthly_vact_vol.php?id=505 (accessed on 29 Jan 2020; in

412    Japanese).

413    Jolivet, R., R. Grandin, C. Lasserre, M. P. Doin, and G. Peltzer (2011), Systematic InSAR tropospheric

414    phase delay corrections from global meteorological reanalysis data, *Geophysical Research Letters*,

415    *38*(17), L17311, doi:10.1029/2011GL048757.

416    Jónsson, S., H. Zebker, P. Segall, and F. Amelung (2002), Fault Slip Distribution of the 1999 Mw 7.1

417    Hector Mine, California, Earthquake, Estimated from Satellite Radar and GPS Measurements,

418    *Bulletin of the Seismological Society of America*, *92*(4), 1377-1389, doi:10.1785/0120000922.

419    Jung, J., D. j. Kim, M. Lavalle, and S. H. Yun (2016), Coherent Change Detection Using InSAR

420    Temporal Decorrelation Model: A Case Study for Volcanic Ash Detection, *IEEE Transactions on*

421    *Geoscience and Remote Sensing*, *54*(10), 5765-5775, doi:10.1109/TGRS.2016.2572166.

422    Kobayashi, T., Y. Morishita, and H. Munekane (2018), First detection of precursory ground inflation of a

423    small phreatic eruption by InSAR, *Earth and Planetary Science Letters*, *491*, 244-254,

424    doi:10.1016/j.epsl.2018.03.041.

425    Lohman, R. B., and M. Simons (2005), Some thoughts on the use of InSAR data to constrain models of

426    surface deformation: Noise structure and data downsampling, *Geochemistry, Geophysics,*

427    *Geosystems*, *6*(1), doi:10.1029/2004GC000841.

428    Lu, Z., T. Masterlark, J. Power, D. Dzurisin, and C. Wicks (2002), Subsidence at Kiska Volcano, Western

429    Aleutians, detected by satellite radar interferometry, *Geophysical Research Letters*, *29*(18), 2-1-2-4,

430    doi:10.1029/2002gl014948.

431    Lundgren, P., S. Usai, E. Sansosti, R. Lanari, M. Tesauro, G. Fornaro, and P. Berardino (2001), Modeling

432    surface deformation observed with synthetic aperture radar interferometry at Campi Flegrei caldera,

433    *Journal of Geophysical Research: Solid Earth*, *106*(B9), 19355-19366, doi:10.1029/2001jb000194.

434    Manconi, A., T. R. Walter, and F. Amelung (2007), Effects of mechanical layering on volcano

435        deformation, *Geophysical Journal International*, *170*(2), 952-958, doi:10.1111/j.1365-

436        246X.2007.03449.x.

437    McTigue, D. F. (1987), Elastic stress and deformation near a finite spherical magma body: Resolution of

438        the point source paradox, *Journal of Geophysical Research: Solid Earth*, *92*(B12), 12931-12940,

439        doi:10.1029/JB092iB12p12931.

440    Miyagi, Y., T. Ozawa, and Y. Kohno (2013), Crustal Deformation Associated with the 2011 Eruption of

441        Shinmoe-dake in Kirishima Volcano Group, Southwestern Japan, Detected by DInSAR and GPS

442        Measurements, *BULLETIN OF THE VOLCANOLOGICAL SOCIETY OF JAPAN*, *58*(2), 341-351,

443        doi:10.18940/kazan.58.2_341 (in Japanese).

444    Miyagi, Y., T. Ozawa, T. Kozono, and M. Shimada (2014), Long-term lava extrusion after the 2011

445        Shinmoe-dake eruption detected by DInSAR observations, *Geophysical Research Letters*, *41*(16),

446        5855-5860, doi:10.1002/2014GL060829.

447    Morishita, Y., and T. Kobayashi (2018), Ground Surface Displacement of Kirishima Volcano Group

448        Detected by ALOS-2 InSAR Time Series Analysis and Effect of Atmospheric Noise Reduction,

449        *Journal of the Geodetic Society of Japan*, *64*, 28-38, doi:10.11366/sokuchi.64.28 (in Japanese).

450    Muffler, L. J. P., D. E. White, and A. H. Truesdell (1971), Hydrothermal Explosion Craters in

451        Yellowstone National Park, *GSA Bulletin*, *82*(3), 723-740, doi:10.1130/0016-

452        7606(1971)82[723:Heciyn]2.0.Co;2.

453    Nakaboh, M., H. Ono, M. Sako, Y. Sudo, T. Hashimoto, and A. W. Hurst (2003), Continuing deflation by

454        fumaroles at Kuju Volcano, Japan, *Geophysical Research Letters*, *30*(7), doi:10.1029/2002gl016047.

455    Nakada, S., M. Nagai, T. Kaneko, Y. Suzuki, and F. Maeno (2013), The outline of the 2011 eruption at

456        Shinmoe-dake (Kirishima), Japan, *Earth, Planets, and Space*, *65*, 475-488,

457        doi:10.5047/eps.2013.03.016.

458    Nakamichi, H., Y. Yamanaka, T. Terakawa, S. Horikawa, T. Okuda, and F. Yamazaki (2013), Continuous

459        long-term array analysis of seismic records observed during the 2011 Shinmoedake eruption activity

460    of Kirishima volcano, southwest Japan, *Earth Planets Space*, *65*(6), 551-562,

461    doi:10.5047/eps.2013.03.002.

462    Nakao, S., Y. Morita, H. Yakiwara, J. Oikawa, H. Ueda, H. Takahashi, Y. Ohta, T. Matsushima, and M.

463    Iguchi (2013), Volume change of the magma reservoir relating to the 2011 Kirishima Shinmoe-dake

464    eruption—Charging, discharging and recharging process inferred from GPS measurements, *Earth*

465    *Planets Space*, *65*(6), 505-515, doi:10.5047/eps.2013.05.017.

466    Narita, S., and M. Murakami (2018), Shallow hydrothermal reservoir inferred from post-eruptive

467    deflation at Ontake Volcano as revealed by PALSAR-2 InSAR, *Earth Planet Sp*, *70*(1), 191,

468    doi:10.1186/s40623-018-0966-6.

469    Narita, S., T. Ozawa, Y. Aoki, M. Shimada, M. Furuya, Y. Takada, and M. Murakami (2020), Precursory

470    ground deformation of the 2018 phreatic eruption on Iwo-Yama volcano, revealed by four-

471    dimensional joint analysis of airborne and spaceborne InSAR, *Earth Planet Sp*, *72*(1), 145,

472    doi:10.1186/s40623-020-01280-5.

473    Newhall, C. G., and R. Punongbayan (1996), *Fire and mud: eruptions and lahars of Mount Pinatubo,*

474    *Philippines*, Philippine Institute of Volcanology and Seismology Quezon City.

475    Nikkhoo, M., T. R. Walter, P. R. Lundgren, and P. Prats-Iraola (2016), Compound dislocation models

476    (CDMs) for volcano deformation analyses, *Geophysical Journal International*, *208*(2), 877-894,

477    doi:10.1093/gji/ggw427.

478    Ohba, T., K. Nogami, and J.-i. Hirabayashi (1997), Hydrothermal System of the Kirishima Volcanic Area

479    Inferred from the Chemical and Isotopic Composition of Spring Waters and Fumarolic Gases,

480    *BULLETIN OF THE VOLCANOLOGICAL SOCIETY OF JAPAN*, *42*(1), 1-15,

481    doi:10.18940/kazan.42.1_1.

482    Ohba, T., M. Yaguchi, U. Tsunogai, M. Ito, and R. Shingubara (2021), Behavior of magmatic

483    components in fumarolic gases related to the 2018 phreatic eruption at Ebinokogen Ioyama volcano,

484    Kirishima Volcanic Group, Kyushu, Japan, *Earth Planet Sp*, *73*(1), 81, doi:10.1186/s40623-021-
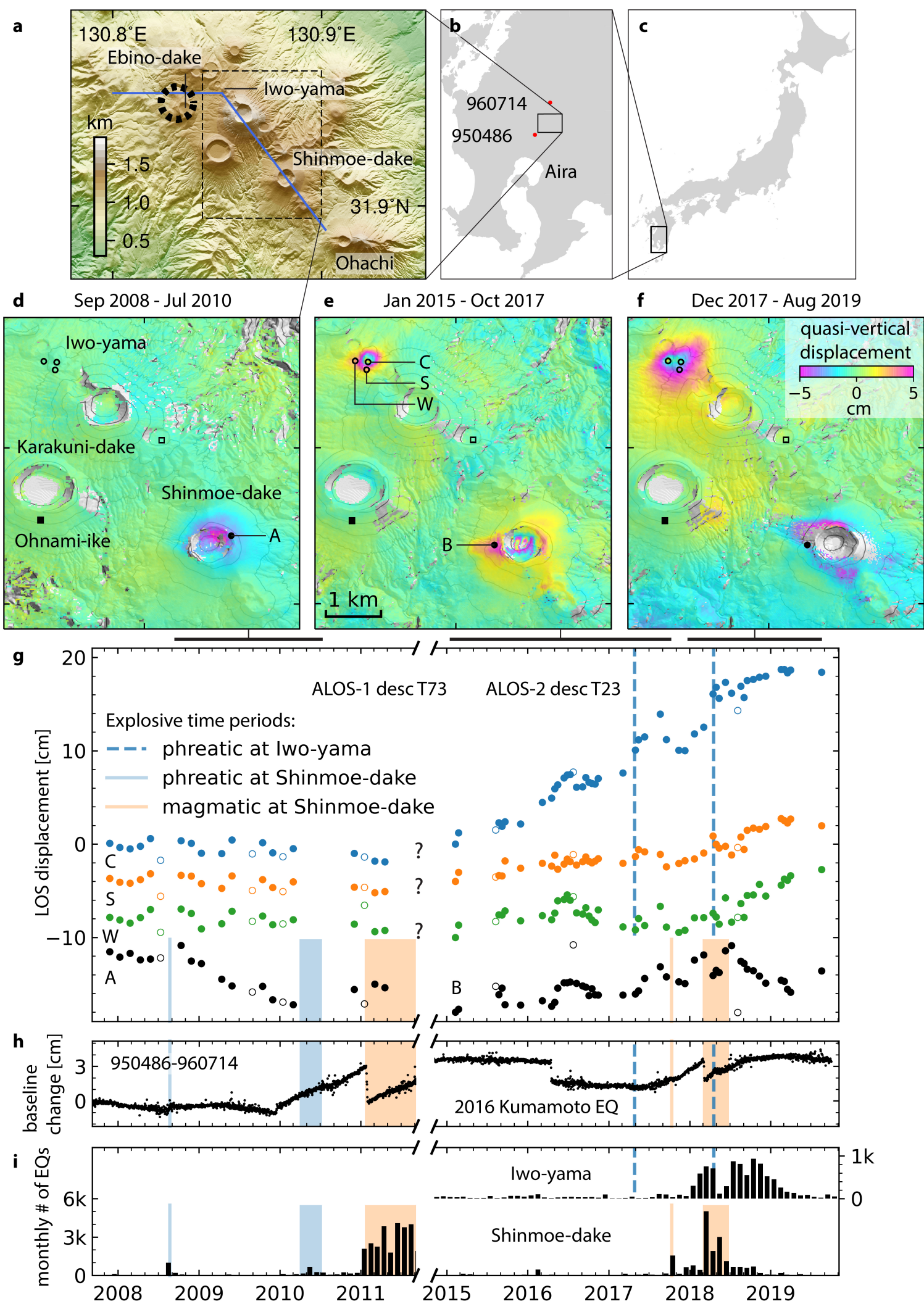
485    01405-4.

486  Ozawa, T., and T. Kozono (2013), Temporal variation of the Shinmoe-dake crater in the 2011 eruption

487      revealed by spaceborne SAR observations, *Earth Planets Space*, *65*(6), 527-537,

488      doi:10.5047/eps.2013.05.004.

489  Rosen, P. A., E. Gurrola, G. F. Sacco, and H. Zebker (2012), The InSAR scientific computing

490      environment, paper presented at EUSAR 2012, 23-26 April 2012.

491  Shimono, T., H. Minami, Y. Nishii, H. Ohno, and K. Watanabe (2011), Observation of volcanic crater of

492      Mt. Kirishima (Shinmoedake) by airborne SAR, *J Geogr Surv Inst*, *121*, 189-194.

493  Stix, J., and J. M. de Moor (2018), Understanding and forecasting phreatic eruptions driven by magmatic

494      degassing, *Earth Planet Sp*, *70*(1), 83, doi:10.1186/s40623-018-0855-z.

495  Suzuki, Y., M. Nagai, F. Maeno, A. Yasuda, N. Hokanishi, T. Shimano, M. Ichihara, T. Kaneko, and S.

496      Nakada (2013), Precursory activity and evolution of the 2011 eruption of Shinmoe-dake in Kirishima

497      volcano-insights from ash samples, *Earth, Planets, and Space*, *65*, 591-607,

498      doi:10.5047/eps.2013.02.004.

499  Tajima, Y., Y. Matsuo, T. Shoji, and T. Kobayashi (2014), Eruptive History of Ebinokogen Volcanic

500      Area of Kirishima Volcanoes for the Past 15,000 Years in Kyushu, Japan, *BULLETIN OF THE*

501      *VOLCANOLOGICAL SOCIETY OF JAPAN*, *59*(2), 55-75, doi:10.18940/kazan.59.2_55 (in Japanese).

502  Tajima, Y., S. Nakada, F. Maeno, T. Huruzono, M. Takahashi, A. Inamura, T. Matsushima, M. Nagai,

503      and J. Funasaki (2020), Shallow Magmatic Hydrothermal Eruption in April 2018 on Ebinokogen

504      Ioyama Volcano in Kirishima Volcano Group, Kyushu, Japan, *Geosciences*, *10*(5), 183,

505      doi:10.3390/geosciences10050183.

506  Takeo, M., Y. Maehara, M. Ichihara, T. Ohminato, R. Kamata, and J. Oikawa (2013), Ground

507      deformation cycles in a magma-effusive stage, and sub-Plinian and Vulcanian eruptions at Kirishima

508      volcanoes, Japan, *Journal of Geophysical Research: Solid Earth*, *118*(9), 4758-4773,

509      doi:10.1002/jgrb.50278.

510  Tsukamoto, K., K. Aizawa, K. Chiba, W. Kanda, M. Uyeshima, T. Koyama, M. Utsugi, K. Seki, and T.

511      Kishita (2018), Three-Dimensional Resistivity Structure of Iwo-Yama Volcano, Kirishima Volcanic

512     Complex, Japan: Relationship to Shallow Seismicity, Surface Uplift, and a Small Phreatic Eruption,

513     *Geophysical Research Letters*, *45*(23), 12,821-812,828, doi:10.1029/2018gl080202.

514     Ueda, H., T. Kozono, E. Fujita, Y. Kohno, M. Nagai, Y. Miyagi, and T. Tanada (2013), Crustal

515     deformation associated with the 2011 Shinmoe-dake eruption as observed by tiltmeters and GPS,

516     *Earth Planets Space*, *65*(6), 517-525, doi:10.5047/eps.2013.03.001.

517     Wallace, L. M., S. Ellis, K. Miyao, S. Miura, J. Beavan, and J. Goto (2009), Enigmatic, highly active left-

518     lateral shear zone in southwest Japan explained by aseismic ridge collision, *Geology*, *37*(2), 143-146,

519     doi:10.1130/G25221A.1.

520     Wessel, P., W. H. Smith, R. Scharroo, J. Luis, and F. Wobbe (2013), Generic mapping tools: improved

521     version released, *Eos, Transactions American Geophysical Union*, *94*(45), 409-410,

522     doi:10.1002/2013EO450001.

523     Williams, C. A., and G. Wadge (1998), The effects of topography on magma chamber deformation

524     models: Application to Mt. Etna and radar interferometry, *Geophysical Research Letters*, *25*(10),

525     1549-1552, doi:10.1029/98gl01136.

526     Wright, T. J., B. E. Parsons, and Z. Lu (2004), Toward mapping surface deformation in three dimensions

527     using InSAR, *Geophysical Research Letters*, *31*(1), L01607, doi:10.1029/2003GL018827.

528     Yamazaki, K. i., Y. Yamashita, and S. Komatsu (2020), Vault-housed extensometers recorded a rapid

529     initial pulse before precursory magma reservoir inflation related to the 2011 eruption of Shinmoe-

530     dake, Japan, *Earth Planet Sp*, *72*(1), 83, doi:10.1186/s40623-020-01211-4.

531     Yunjun, Z., H. Fattahi, and F. Amelung (2019), Small baseline InSAR time series analysis: Unwrapping

532     error correction and noise reduction, *Computers & Geosciences*, *133*, 104331,

533     doi:10.1016/j.cageo.2019.104331.

534

535     **Figure 1.** Geophysical observations at Kirishima during 2008-2019. (a) Geological setting.

536     Dashed circle: horizontal location of the deep magmatic source (Nakao et al., 2013). Blue lines:

537     cross-section of Fig. 3c. (b-c) Location of Kirishima. Red dots: GPS sites. (d-f) Quasi-vertical

538     displacements (d) during the 2008-2010 phreatic eruptions, (e) before and (f) after the 2017

539     magmatic eruption. Positive value for uplift. Data are wrapped into [-5, 5) cm for display. Black

540     squares: reference points. Contour lines in every 100 m. (g) Line-of-sight (LOS) displacement

541     time-series at Shinmoe-dake and Iwo-yama with respect to the filled and empty black squares,

542     respectively (shifted for display). LOS increase for motion toward the satellite. Empty circles:

543     noisy acquisitions excluded from the average velocity estimation. (h) Baseline change between

544     two GPS stations. (i) Monthly number of earthquakes around Shinmoe-dake and Iwo-yama

545     (JMA, 2019).

546

547     **Figure 2.** Geodetic modeling results at Shinmoe-dake and Iwo-yama. (a-b) Observed LOS

548     displacement at Shinmoe-dake between the 2008-2010 eruptions from ascending and descending

549     orbit. (c-d) Prediction for (a-b) from the CDM. Positive value for motion toward the satellite.

550     Data are wrapped into [-5, 5) cm for display. (e) Profile of observed (empty circles) and

551     predicted (solid lines) displacement from (a-d) and the topography (gray areas). (f-j) Same as (a-

552     e) but for Shinmoe-dake prior to the 2017 eruption. (k-o) and (p-t) Same as (a-e) but for Iwo-

553     yama during 2015-2017 with one CDM and during 2017-2019 with two CDMs, respectively.

554     Black circles in (a-i): Shinmoe-dake crater rim. Black triangles in (c-d): main vent of the 2008-

555     2010 phreatic eruptions (Geshi et al., 2010). Black stars in (c-i): horizontal location of the

556     pressure source centroid. Black vertical lines in (o and t): Iwo-yama crater.

557

558     **Figure 3.** Conceptual model of the magmatic and hydrothermal pressure sources at the Kirishima

559     volcanic complex. (a) Marginal posterior density distributions of depths of pressure source

560     beneath Shinmoe-dake. From left to right: 1) deflation between the 2008-2010 phreatic

561     eruptions, 2) inflation-deflation cycles (filled error bar) during the Vulcanian stage in February

562     2011 (Takeo et al., 2013), 3) deflation (empty error bar) during the 2011-2013 lava extrusion

563     stage (Miyagi et al., 2014) and 4) inflation before the 2017 magmatic eruption. (b) Same as (a)

564     but beneath Iwo-yama for inflation before and after December 2017, respectively. (c) Conceptual

565     model of the plumbing system. The 2008-2010 Shinmoe-dake source has the inferred dimension.

566     The size of the other sources reflects the ratio of their volume changes and the 2008-2010

567     Shinmoe-dake volume change, except for the deep magmatic source. The topography is
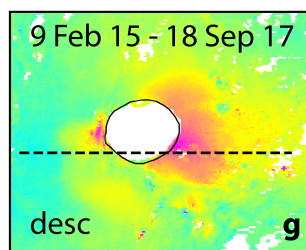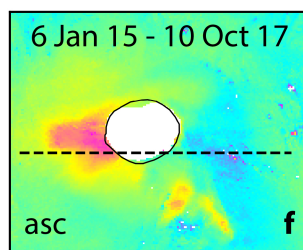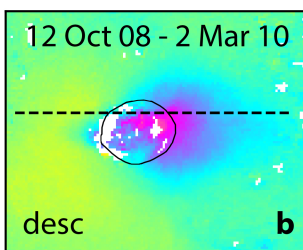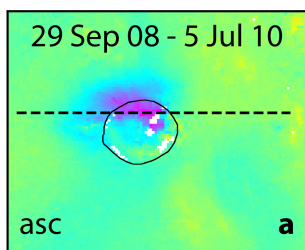
568     vertically exaggerated by 25%.

569

**a** 130.8°E / 130.9°E · Ebino-dake · Iwo-yama · Shinmoe-dake · 31.9°N · Ohachi · km · 1.5 1.0 0.5

**b** 960714 · 950486 · Aira

**c**

**d** Sep 2008 – Jul 2010 · Iwo-yama · Karakuni-dake · Shinmoe-dake · Ohnami-ike · A

**e** Jan 2015 – Oct 2017 · C · S · W · B · 1 km

**f** Dec 2017 – Aug 2019 · quasi-vertical displacement · −5 0 5 · cm

**g**
LOS displacement [cm]

ALOS-1 desc T73 · ALOS-2 desc T23

Explosive time periods:
- - - phreatic at Iwo-yama
— phreatic at Shinmoe-dake
— magmatic at Shinmoe-dake

C · S · W · A · B

**h** baseline change [cm] · 950486-960714 · 2016 Kumamoto EQ

**i** monthly # of EQs · Iwo-yama · Shinmoe-dake · 1k · 0 · 6k · 3k

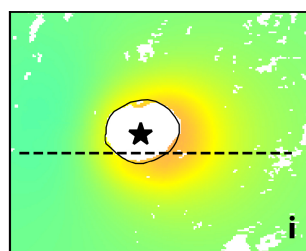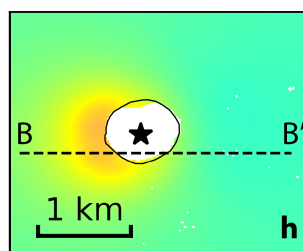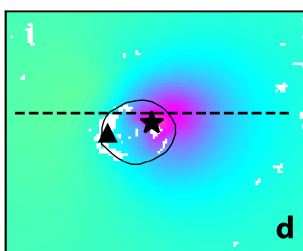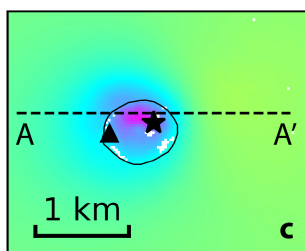2008 2009 2010 2011 2015 2016 2017 2018 2019

Shinmoe-dake

**deflation between the 2008-2010 phreatic eruptions**

**pre-eruptive inflation of the 2017 magmatic eruption**

data

29 Sep 08 - 5 Jul 10 · asc · **a**

12 Oct 08 - 2 Mar 10 · desc · **b**

6 Jan 15 - 10 Oct 17 · asc · **f**

9 Feb 15 - 18 Sep 17 · desc · **g**

model

A — A' · **c**

— **d**

B — B' · **h**

— **i**

1 km

1 km

**e** · asc · desc · A — A'

**j** · asc · desc · B — B'

LOS displacement [cm] · distance [km] · elevation [km]

−5 — 0 — 5
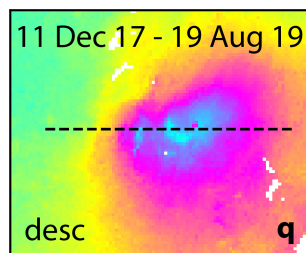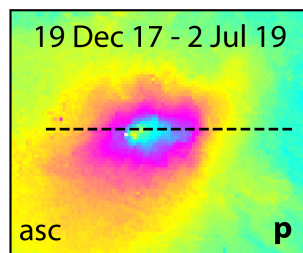
LOS displacement [cm]
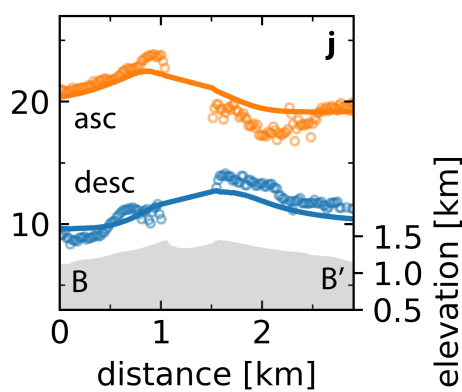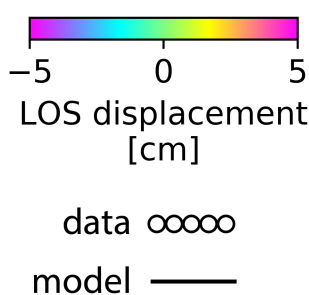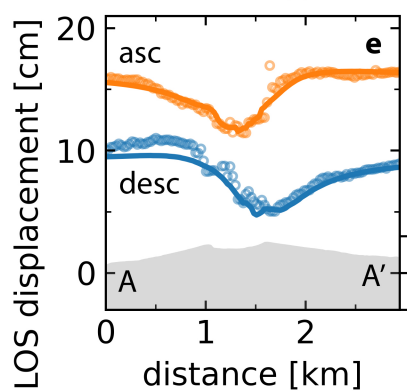
data ○○○○○

model ——

Iwo-yama

**inflation before Oct 2017**

**inflation after Dec 2017**

data

6 Jan 15 - 10 Oct 17 · asc · **k**

9 Feb 15 - 18 Sep 17 · desc · **l**

19 Dec 17 - 2 Jul 19 · asc · **p**

11 Dec 17 - 19 Aug 19 · desc · **q**

model

C — C' · **m**

— **n**

C — C' · **r**

— **s**

800 m

800 m

**o** · asc · desc · C — C'

**t** · asc · desc · C — C'

LOS displacement [cm] · distance [km] · elevation [km]

**a** Shinmoe-dake (1,421 m)

2008-2010    2011-2013    2014-2017

**b** Iwo-yama (1,313 m)

2014-2017    2017-2019

depth [km] below the summit

fixed

**c**

● hydrothermal
● magmatic

Iwo-yama

Shinmoe-dake

*Koshiki-dake*

*Karakuni-dake*

*Ebino-dake*

*Ohata-ike*

*Ryuo-dake*

*Ya-dake*

depth a.s.l. [km]

2015 - 2019
Dec 2017 - 2019

2008-2010

Jan - Feb 2011
Nov 2011 - 2013
2015 - 2017

Dec 2009 - Nov 2011
Jul 2017 - Mar 2018

31.98° N

31.95° N

130.92° E